Process Phenomena Influencing the Tensile and Anisotropic Characteristics of Additively Manufactured Maraging Steel

Barry Mooney[a], Kyriakos I. Kourousis[a,*], Ramesh Raghavendra[b], Dylan Agius[c]

[a]*School of Engineering, University of Limerick, Ireland, V94 T9PX*
[b]*South Eastern Applied Materials Research Centre (SEAM), Waterford Institute of Technology, Ireland, X91 TX03*
[c]*School of Aerospace, Mechanical and Manufacturing Engineering, RMIT University, Melbourne VIC 3000, Australia*

Abstract

The tensile mechanical properties and anisotropy levels of identical test-coupons, fabricated from maraging steel 300 (MS300) using two alternative EOS EOSINT M280 Additive Manufacturing (AM) systems, have been examined. The mechanical performance variations resulting from process differences between the two suppliers and the part's build volume orientation (0°, 45°, 90°) are investigated. Significant microstructural discrepancies, affecting mechanical performance, plasticity and anisotropy levels, have been observed in the as-built samples obtained from the two suppliers. A difference in the angle of the laser scan strategy, in conjunction with unfavourable powder feedstock characteristics, are understood to have had a profound influence on the plasticity and anisotropy divergences observed in the AM MS300 alloy. Plastic anisotropy levels can be largely reduced through application of aging heat-treatments, however, a degree of transverse strain anisotropy is likely to remain due to the AM alloy's fabrication history. Moreover, in this work both the anisotropic and elasticity tensors for this material are derived. These tensors can be used by researchers working on modelling and simulation of the MS300 mechanical properties.

Keywords: additive manufacturing, 3D printing, maraging steel, anisotropy, heat treatment, strength, ductility.

1. Introduction

Maraging steel 300 (MS300) is a high-strength Fe-Ni based alloy which, in powder form, is used widely as a feedstock for laser additive manufacturing (AM). MS1 is one such powder developed by EOS for their *Direct Metal*

*Corresponding author
Email address: Kyriakos.Kourousis@ul.ie (Kyriakos I. Kourousis)

Laser Sintering (DMLS) systems. The alloy's high-strength, combined with its agreeableness to laser-synthesis, facilitates the rapid production of geometrically complex structures which have load-bearing capabilities and can easily achieve high-density and chemically homogeneous microstructures [1, 2, 3]. As AM technology matures, it is progressively becoming a viable option for serial production of structure-critical engineering components [4, 5]. Key to this successful advancement is a clear understanding of the factors which influence the metallurgical soundness of the produced parts.

An important aspect for the serial production of AM parts is the ability to achieve consistent and repeatable mechanical properties outputs for identical parts produced on alternative machines, however, very limited published research exists on the repeatability of mechanical behaviour in AM-produced metals [6, 7, 8, 9]. Indeed, there is variation in the EOS-reported as-built MS1 mechanical properties for identical test-coupons fabricated on EOS DMLS equipment [10, 11], but also among MS300 properties reported in the open literature for contrasting test-coupon geometries which have been fabricated on EOS and other metal AM systems [12, 13, 14][15, 16, 9, 17, 2, 18, 19, 20]. The spread of the as-built tensile properties reported across these studies (i.e. elasticity modulus (E): 150-194 GPa [11, 15]; yield strength ($R_{p0.2}$): 768-1214 MPa [18, 16]; tensile strength (R_m): 1010-1325 MPa [15, 18]; and elongation to fracture (A_t): 6.1-14.3 % [2, 13]) is a measure of the variability observed. This highlights the need for a deeper understanding of the factors that affect the reproducibility of AM parts, since engineers seeking to use this advantageous technology for structure-critical designs require a greater control of the achievable mechanical properties.

In this paper, we examine the material characteristics, microstructures, tensile properties, and anisotropy variation of identical MS300 test-coupons which have been fabricated in three build orientations (0°, 45°, and 90°), on two EOS EOSINT M280 AM machines belonging and operated by different users. For this purpose, the relationship between the AM process phenomena and the resulting mechanical properties, including plastic anisotropy, has been Moreover, in this work both the anisotropic and elasticity tensors for this material are derived. These tensors can be used by researchers working on modelling and simulation of the MS300 mechanical properties.

2. Material and methods

2.1. Fabrication of samples

Test coupons were fabricated from MS1 powder feedstock on two EOS *EOSINT M280* AM systems belonging and operated by different users, denoted as Supplier 1 and Supplier 2. Both AM systems were controlled using the EOS-predefined set of parameters *MS1 Performance 2.0*, which administers $40\mu m$ layer-thickness and has been optimized by EOS for the fabrication of MS1 components. The chemical composition of the MS1 material is presented in Table 1, along with the results of the energy dispersive X-ray (EDX) analysis, which

were obtained with a *Hitachi SU 70* scanning electron microscope (SEM), fitted with an *Oxford Instruments* EDX attachment. A close agreement between the Supplier 1 and 2 SEM-EDX values and the EOS published values [11] for MS1 is observed, which also confirms that the powder material used is in line with the manufacturer's (EOS) specifications.

Table 1: Chemical composition (%wt) of MS1, the 18Ni (300) grade maraging steel powder supplied by EOS (GmbH) [11] with SEM-EDX analysis results for the main comprising elements.

	Ni	**Mo**	**Co**	**Ti**	**Al**	**Cr**	**Si**	**Mn**	**C**	**Fe**
MS1 [11]	17-19	4.5-5.2	8.5-9.5	0.6-0.8	0.05-0.15	0-0.5	0-0.1	0-0.1	0-0.03	Bal.
Supplier 1-EDX	18.14	5.67	8.94	0.87	-	-	-	-	-	Bal.
Supplier 2-EDX	17.96	5.65	9.08	1.05	-	-	-	-	-	Bal.

Four sets of test specimens, orientated at three angles [0° (horizontal), 45° (inclined), and 90° (vertical)] between their longitudinal axis and the build platform, were produced on each machine. This facilitated an investigation of the influence of build orientation on property anisotropy. For this purpose, a rectangular-shaped tensile test specimen having uniform cross-section at gage and meeting the requirements of the ASTM-E8M standard [21] was selected. The finished specimen geometry, dimensions and tolerances are shown in Figure 1a. This specimen design allowed for the measurement of both lateral and axial elastic and plastic strains whilst under tensile loading. A machining allowance of 0.5mm was included to ensure that a uniform and high-quality surface finish, appropriate for the tensile testing of high-strength specimens [21], could be achieved. After the AM build, the DMLS parts were processed through a single-cycle precision computer numerically controlled (CNC) wire electrical discharge machining (EDM) profiling and surface-grinding operations.

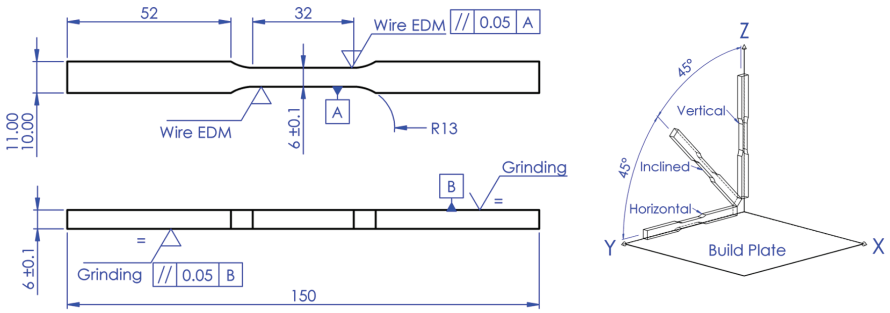

(a) (b)

Figure 1: (a) Showing the finish-machined specimen geometry, and (b) the AM build volume coordinate system and test-specimen build orientations.

2.2. Heat-treatment

High strength is achieved in MS300 through a second phase precipitation of inter-metallic compounds (Ni_3Ti, Ni_3Mo, Fe_2Mo and Fe_7Mo_6) for which a disperse concentration of fully dissolved hardening elements in solid solution is necessary [22, 23, 24]. In contrast to conventionally produced MS300, and by reason of the rapid cooling rates (circa 10^3 to 10^8 $K.s^{-1}$), the DMLS process provides a solid solution with full potential for precipitation strengthening [23]. EOS therefore recommend a straightforward isothermal aging heat-treatment of 6 hours at $490°C$ [11] which allows a populous dispersion of dislocation hindering precipitates to form, and leads to the alloy's characteristic high strength (circa 2,000 MPa) and hardness.

In this study, three sets of specimens obtained from each M280 machine, were aged at $490°C$ for durations 4, 6 and 8 hours (h), while the remaining two sets were kept in the as-built condition. The aging parameters were chosen to investigate the influence of heat-treatment on mechanical properties and anisotropy levels, and to validate the EOS recommendation.

2.3. Characterization

Archimedes' Principle density measurements were performed on as-built samples obtained from each DMLS machine, and for each build-orientation, using a *Sartorius Quintix* analytical balance which was fitted with accessory YDK03 density determination kit. The measurement procedure followed the guidelines present in the ASTM B962-17 [25] standard.

Metallographic samples were obtained from arbitrary sections of the fractured coupon's grip-ends, then mounted with phenolic compound, and polished using standard finishing steps. The sectioned plane was taken perpendicular to the materials tensile loading axis in each case, and the etched microstructure (150mL H_2O; 50mL HCl; 25mL HNO_3; 1g $CuCl_2$) was then inspected using an *Olympus BX60* Optical microscope.

Porosity was examined via X-ray Computed Tomography (CT) scans, performed using a General Electric *VTOMEX L300, Nanotom S* instrument operating at 180kV, $80\mu A$, $250\mu s$ and with a resolution of $13.4\mu m$. Digital inspection of the porosity network, and a quantitative evaluation of the size and distribution of pores was completed using Thermo Fisher Scientific's *Avizo* software [26].

Vickers hardness indents were applied perpendicular to the metallographic sample's sectioned plane using a *Zwick ZHV* hardness tester which had been calibrated with a standard test block to the requirements of ASTM E92-17 [27]. Twenty (20) measurements were performed on each of the mounted and polished samples, and the results and test statistics were computed using the R statistical software package [28].

Tensile testing was conducted at room-temperature in a *Zwick/Roell (Dartec) M1000/RK* servo-hydraulic testing machine equipped with 100kN capacity load cell and fitted with ±100kN fatigue rated hydraulic wedge grips. The test procedure was fully compliant with the ASTM E8M standard [21]. Among other test

requirements, this standard prescribes stressing/ straining/ displacement rates for deriving reliable and consistent mechanical properties data. The test was initially controlled (via a 9600 series controller) to the elastic stressing rate of 10.34 MPa/s, using strain control from the extension feedback channel (Epsilon model 3542-025M-050-ST). Upon detection of yield, the test-rate maintained a constant plastic strain rate of $6.25 \times 10^{-4}/s$ controlled via the stroke feedback channel. At the end of the yield (detected from either reaching a 5% increase in stress, or an absolute strain limit of 2%), the test-velocity was commanded by a third rate, the tensile strength (R_m) rate: 0.0068/s. This strain rate was maintained to peak force through failure.

Concurrently, a non-contact full-field displacement measurement was performed using *LaVision's* portable 3D Digital Image Correlation (DIC) apparatus complete with *StrainMaster* software [29]. This involved the application of a non-repeating isotropic acrylic speckle pattern (dark black speckles on a bright white background) onto the gage surface of the specimen and capturing a sequence of images throughout each tensile test at a periodic rate of 5Hz (i.e. from zero applied load until fracture). The purpose of the speckle pattern is to provide a unique signature pixel arrangement from which the specimen's displacement field can be digitally tracked throughout the tensile test. Poisson (ν) and plastic strain ratios (R-values) were calculated from the DIC determined strain data in accordance with ASTM test methods E132-04 [30] and E517-18 [31]. R-value is the ratio of true width strain (ε_w) to true thickness strain (ε_t), given by Eq. 1, with both strains calculated after tensile plastic flow was induced.

$$R\ value = \frac{\varepsilon_w}{\varepsilon_t} \tag{1}$$

The R-value was employed to quantify the strain plastic anisotropy (non-uniform transverse straining), which typically is anticipated in AM-fabricated parts. The complete experimental configuration is illustrated in Figure 2 (each feature discussed in this section is indicated on this figure).

3. Results and discussion

3.1. Microstructures and density

Representative micrographs are presented for the individual build orientations of parts obtained from each supplier in Figure 3. A distinct dissimilarity was observed in the microstructures of the sectioned vertically orientated (90°) parts. As shown in Figures 3c and 3f, different laser scan strategies were administered by each M280 system during the fabrication process, despite the fact that the MS1 Performance 2.0 set of parameters was used by both suppliers. Supplier 1 specimens were fabricated with a 67° line scan rotation between successive build layers, whereas Supplier 2 specimens display a 90° scan rotation. Other researchers [3, 32] have reported a layer-wise scan rotation angle of 67° when employing MS1 optimized parameters on similar EOS machines. Nevertheless, these limited literature-reported findings do not exclude the existence of strategies with other scan rotation angles (as found in this study).

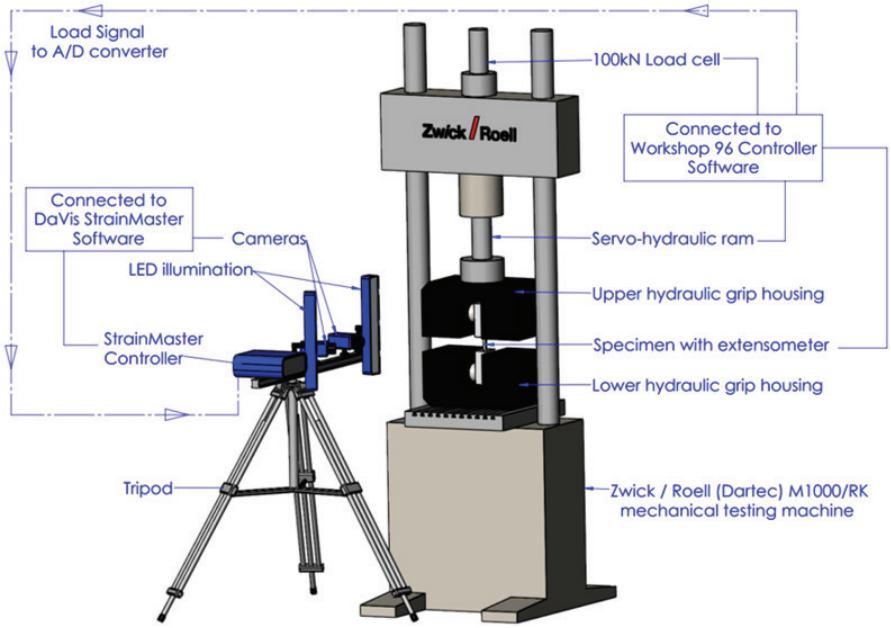

Figure 2: Configuration of tensile test set-up including the 3D Digital Image Correlation (DIC) apparatus which allowed concurrent determination of test-specimen width and axial strains.

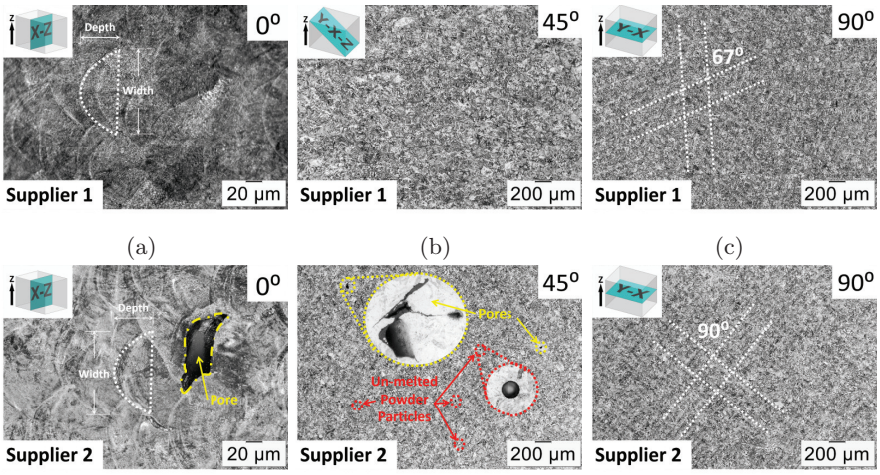

Figure 3: Representative optical micrographs of samples fabricated in three build-orientations on two EOSINT M280 systems (Supplier 1 and Supplier 2): (a) and (d) horizontal (0°); (b) and (e) inclined (45°); and (c) and (f) vertical (90°).

Comparable melt-pool proportions, which are reflective of the applied laser energy input (< 200W), can be observed in the horizontal cross-sections shown in Figures 3a and 3d. In particular, melt-pool depths 35-55μm corresponding to the applied 40μm layer thickness, and widths 45-70μm suggesting a laser focus diameter of $\approx 60\mu m$, were observed. Supplier 2 micrographs revealed persistent defects in the form of pores and un-melted powder particles as indicated in Figures 3d and 3e by dotted lines. In connection, inferior density was recorded for Supplier 2 specimens as reported in Table 2. Nonetheless, all the reported density values fall within the EOS quoted density range of 8.0 - 8.1 g/cm^3 [11]. The determined density values (Table 2) do not provide sufficient evidence to suggest that part density is influenced by the AM build orientation, however, it is worth noting for the proceeding sections that the Supplier 2 horizontal samples, which exhibited a relatively high degree of porosity in their microstructures, also obtained the lowest overall density values.

Table 2: Comparing the density values of MS300 samples obtained from two EOS M280 DMLS systems for the as-built Horizontal (0°), Inclined (45°), and Vertical (90°) build orientations.

	Density, ρ (g/cm^3)		
	0°	**45°**	**90°**
Supplier 1	8.051	8.050	8.049
Supplier 2	8.028	8.031	8.034

It is believed that the observed microstructural defects may be caused by the powder feedstock characteristics, which is consistent with the findings recently reported by Quinn et al. [33]. In particular, smaller spherical granules permit high packing efficiencies and are readily consumed during recoating. Contrastingly, larger granules are more likely to get pushed cross-platform into the system's collection chamber. Therefore, successive recycling and collection of powder granules following completed AM builds increases the percentile volume of larger and agglomerated powder particles in the feedstock [33]. When used in subsequent AM builds, the affected powder will impede flow behaviour due to inter-particle friction during the recoating process, lead to reduced packing efficiencies, and interact differently with the laser-beam [34]. These factors may have contributed to the porosities and un-melted particles which were observed in the Supplier 2 micrographs. Accordingly, the importance of appropriate powder sieving and quality control techniques is evident, since these will influence the feedstock characteristics, and ultimately induce microstructural defects in AM fabricated alloys. It is, however, noted that the feedstock quality may not be the sole responsible for the development of microstructural defects, as the role of the wider (90°) scan rotation angle has to be examined as well (both separately and in conjunction with the powder quality). To that end, further work is planned, to fully characterise the effect of alternative scan-strategies on the microstructural integrity and anisotropy of MS300 parts fabricated with the EOS machines.

3.2. X-ray CT-scans

The porosity level observed in the Supplier 2 samples mandated a more comprehensive evaluation using X-ray CT-scans. The re-constructed scans are presented in Figure 4, while Figure 5 presents histograms of the pore size distribution for all three build orientations examined in this study. The scans were performed on as-built material surrounding the fractured surface to help identify if a coalescence of pores led to crack initiation. While no evidence of this was found, there appears to be independent porosity variation due to part orientation within the build volume. The horizontal (0°) sample displayed a lower relative density, and a much greater proportion of larger pores when compared to the inclined (45°) and vertically orientated (90°) samples. The results suggest that the achievable relative density is a function of the powder's quality, and the part's build-platform projected area (i.e. layer-wise cross-sectional area), since the horizontal layers had a significantly larger build-platform projection and were therefore more likely to be affected by powder packing deficiencies during recoating.

Although the horizontal (0°) sample exhibited a comparatively large degree of porosity, the relative density of the analysed volume of MS300 material remained higher than 99.96% which verifies the alloy's suitability for AM fabrication and welding [1, 2, 35]. It is also of note that each of the samples displayed a populous dispersion of sub $\emptyset 40 \mu m$ sized defects which is an anticipated finding for this, previously stressed, material.

3.3. Mechanical properties

Tensile stress (σ) versus strain (ε) curves, Vickers hardness aging curves, and their associated mechanical property values are presented in Figures 6, 7a, and Table 3 respectively. Significant anisotropy, and an appreciable supplier related variation has been confirmed in both the as-built and aged MS300 stress-strain curves. In particular, the largest and most obvious strength and ductility divergence can be seen in the as-built inclined (45°) specimens' $\sigma - \varepsilon$ curves. Although achieving a 218MPa (22%) superior yield strength ($R_{p0.2}$), the sample fabricated with 67° laser scan rotation (Supplier 1) displayed an unusual σ versus ε trajectory. As shown by the solid green curve in Figure 6a, an uneven material response during plastic deformation culminated in failure at $\approx$ 57% less elongation (i.e. a reduction of 9.1%) when compared to the Supplier 2 specimen (dashed green curve), which had been fabricated with the 90° laser scan rotation. Remarkably, these samples have comparable hardness values, which indicates that hardness measurements alone can provide insufficient information for the assessment of the mechanical properties. This also explains why similar observations have not been reported in the AM MS300 research literature to-date.

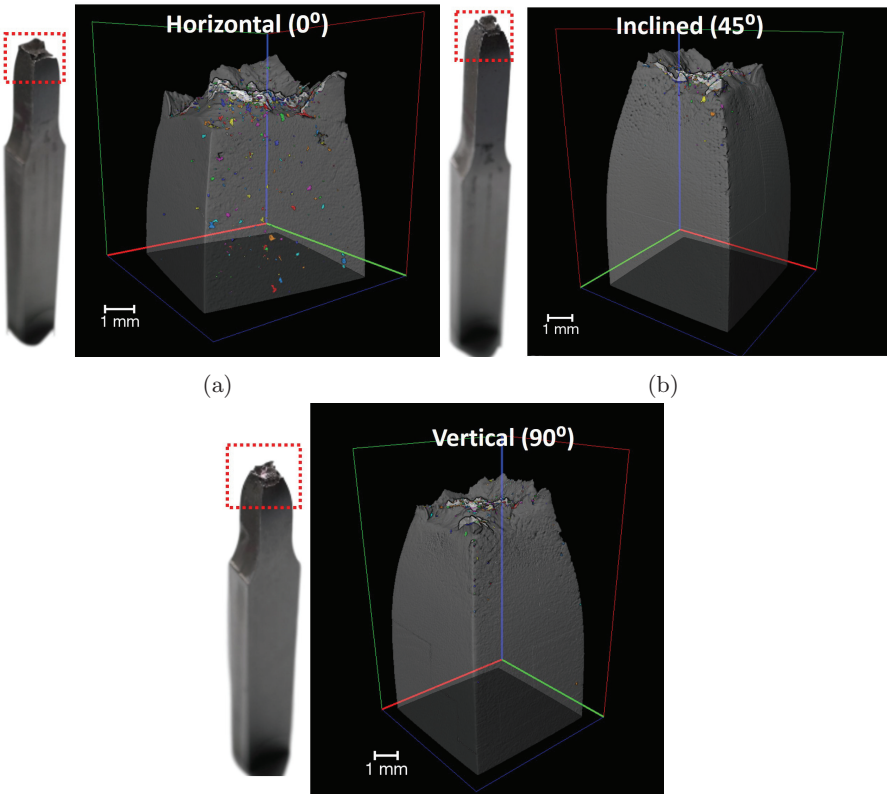

(a) (b)

(c)

Figure 4: Transparent X-ray CT reconstructions showing micro-pores in a volume of DMLS as-built MS300 for build-orientations: (a) Horizontal (0°); (b) Inclined (45°); and (c) Vertical (90°).

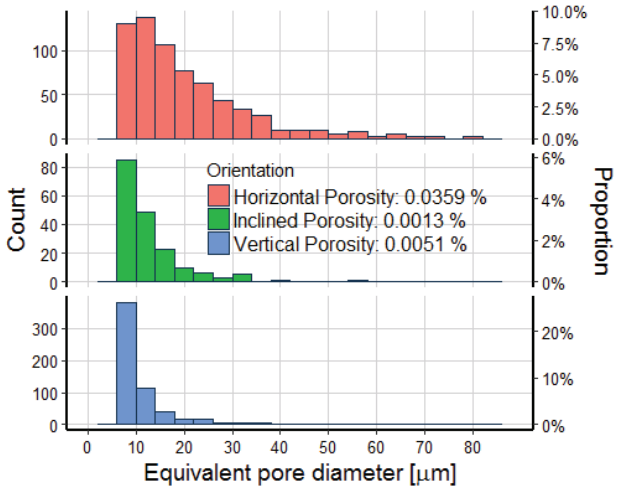

Figure 5: Histograms of the pore size distribution in the as-built MS300 alloy which has been fabricated in three AM build-orientations: Horizontal (0°); Inclined (45°); and Vertical (90°).

Table 3: Mechanical properties data retrieved from tensile and Vickers hardness testing of MS300 produced by DMLS (Elasticity modulus (E); Poisson ratio (ν); Yield strength ($R_{p0.2}$); Tensile strength (R_m); Elongation to fracture (A_t); Reduction in area (Z); and Vickers hardness (HV)). EOS reference data [11] are shown with italics fonts.

Data	Heat-Treatment	Orien-tation	E [GPa]	ν	$R_{p0.2}$ [MPa]	R_m [MPa]	A_t [%]	Z [%]	HV_{30kgf} [kg/mm^2]
EOS	*EOS As-Built[11]*	*0°*	*160*±25	-	*1050*±100	*1100*±100	*10*±4	-	*(310-360)*
		90°	*150*±20	-	*1000*±100	*1100*±100	*10*±4	-	*(310-360)*[a]
	EOS Aged[11] 6h @ 490°C	*0°*		-				-	
		90°	*180*±20	-	*1990*±100	*2050*±100	*4*±2	-	*(>513)*
Supplier 1	As-Built	0°	161	0.24	1069	1174	15.7	56	382
		45°	140	0.29	991	1144	6.8	56	327
		90°	122	0.35	892	1057	13.8	62	375
	4h @ 490°C	0°	182	0.33	1961	2004	8.6	33	603
		45°	185	0.31	1895	1963	8.0	28	595
		90°	180	0.32	1875	1928	5.9	24	599
	6h @ 490°C	0°	178	0.40	1901	1958	5.9	19	602
		45°	183	0.28	1925	1984	4.4	10	603
		90°	178	0.28	1893	1958	6.1	22	599
	8h @ 490°C	0°	183	0.34	1969	2020	8.3	32	608
		45°	184	0.29	1930	1993	7.8	29	606
		90°	180	0.32	1912	1978	4.2	21	615
Supplier 2	As-Built	0°	150	0.34	1028	1172	12.9	43	369
		45°	136	0.33	773	1053	15.9	60	329
		90°	120	0.38	853	1035	15.1	60	328
	4h @ 490°C	0°	170	0.29	2006	2050	2.3	6	610
		45°	175	0.27	1977	2047	4.4	12	620
		90°	171	0.31	1929	1996	6.1	14	616
	6h @ 490°C	0°	174	0.30	2004	2070	2.9	7	626
		45°	179	0.31	2004	2080	3.9	5	633
		90°	172	0.34	1981	2047	6.2	21	631
	8h @ 490°C	0°	179	0.38	1998	2047	NA[b]	6	636
		45°	178	0.31	2013	2069	3.4	12	635
		90°	170	0.34	2005	2067	5.5	22	640

[a] Brackets indicate approximate hardness conversion numbers per Table 3,[36];
[b] Fracture occurred before end of yield was reached.

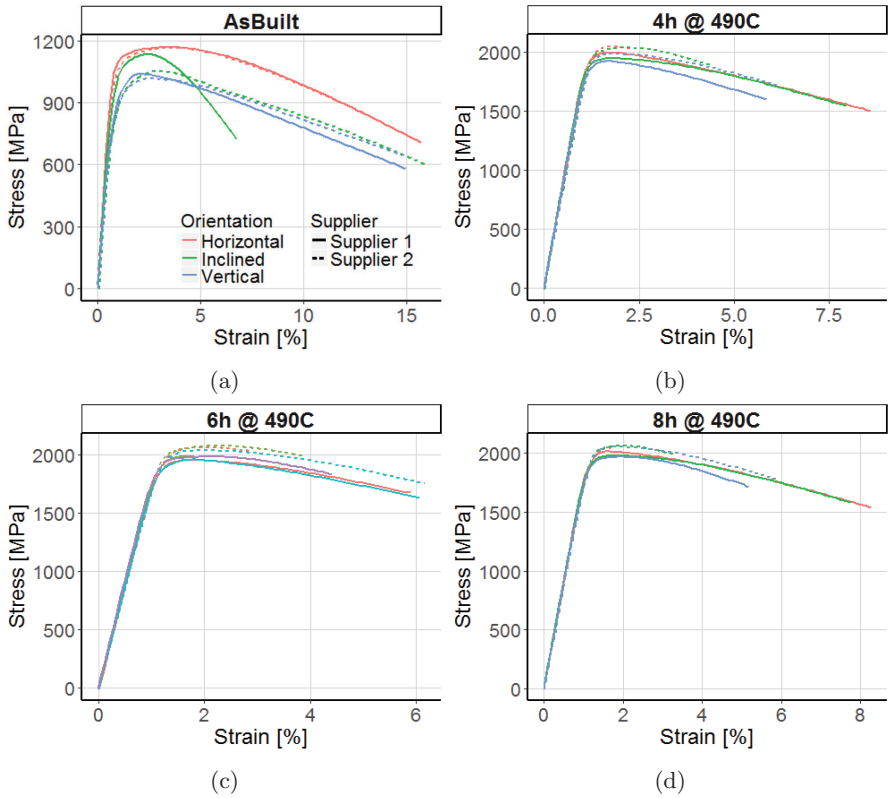

Figure 6: Stress (σ) versus strain (ε) curves comparing as-built and aged MS300 test-specimens which have been fabricated on two EOS EOSINT M280 AM machines belonging and operated by different users.

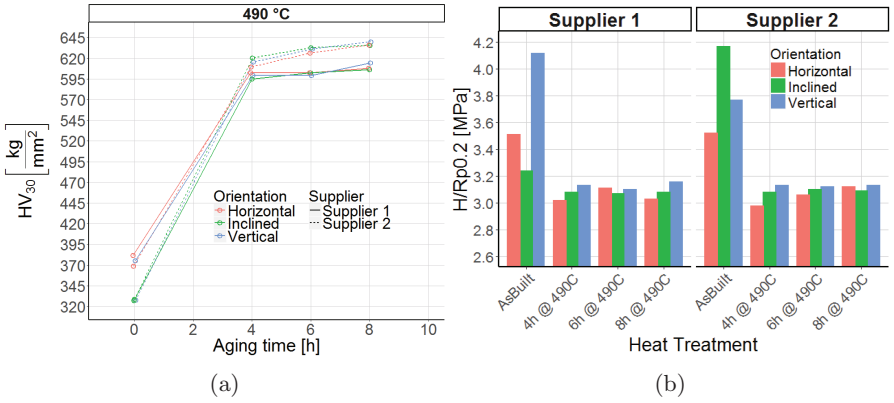

Figure 7: (a) Precipitation strengthening curves; and (b) Ratio of Hardness (H) to Yield Strength for the as-built and heat-treated MS300 examined.

Both sets of as-built samples exhibited a reduction in modulus of elasticity (E) with increasing build-orientation angle. This may be associated with the microstructural pattern developed during build-up of AM layers, since higher E is achieved when the loading direction is parallel to the build layers. AM's distinct three-dimensional (3D) microstructural pattern, visible in Figure 3's micrographs, is brought about by the layer-wise deposition of powder and continuous re-melting/heating of material beneath the melt-pool during build-up.

Overall, Supplier 1 specimens having been fabricated with a 67° layer-wise scan rotation showed higher stiffness and greater strength consistency between build orientations. However, as indicated by the aging and $\sigma - \varepsilon$ curves, greater strength and hardness was achieved in the aged Supplier 2 specimens. The strength and hardness of samples from each supplier continued to rise when the material was aged past the EOS recommended 6h treatment duration. This strength and hardness ascension was accompanied by a reduction in ductility. While in this brittle condition, Supplier 2 samples displayed comparatively erratic and reduced ductility behaviour to those of Supplier 1. Correspondingly, this inferior ductility performance is attributed to the combined consequences of matrix embrittlement due to coarsened precipitates, and the presence of microstructural pores/un-melted particles, which jointly act as sites for crack nucleation [17, 2, 23, 3, 37, 38, 39].

When comparing the experimental mechanical properties against the EOS published data (Table 3), both as-built vertical (90°) parts underperformed in terms of elasticity modulus (≈19% lower), and yield strength (≈13% lower). Upon aging, the alloy gained remarkable strength (>87% increase) and hardness (>75% increase), and most mechanical property values fell within the EOS published confidence bands. This MS300 reflection demonstrates the outstanding effectiveness of the precipitate development towards obstructing and retarding the movement of dislocations in the lattice, but also towards suppressing anisotropic material behaviour.

To compare the mechanical and anisotropic characteristics of samples from either supplier, a relationship between *hardness* (H) and yield strength ($R_{p0.2}$), which is based on similar empirical relationships used for other metals, was devised from the available test data. In particular, the typical linear rule-of-thumb for a broad range of metallic alloys given by Eq. 2 [40] has been used.

$$H \approx 3 \times R_{p0.2} \tag{2}$$

Where hardness (H), described as the indenter force divided by the projected area of the indent (in MPa) is determined by Eq.3.

$$H = HV_{30} \times 9.81 m/s^2 \tag{3}$$

Where HV_{30} represents the Vickers hardness value. The experimental relationships, presented in Figure 7b, demonstrate the extent of as-built stress anisotropy in the DMLS alloy due to supplier variation and part orientation. The most prominent discrepancies take place between as-built samples obtained

from either supplier. This supplier related anisotropy variation may be attributed to the alternative scan strategies employed on either AM machine, and suggests that the scan rotation angle has a significant effect on mechanical anisotropy. Following the application of the aging heat-treatments, the degree of stress anisotropy is dramatically reduced by the presence of hard second phase precipitate particles [41], and Equation 2 is satisfied. Nevertheless, the anisotropy developed during the fabrication process is not fully abolished following aging.

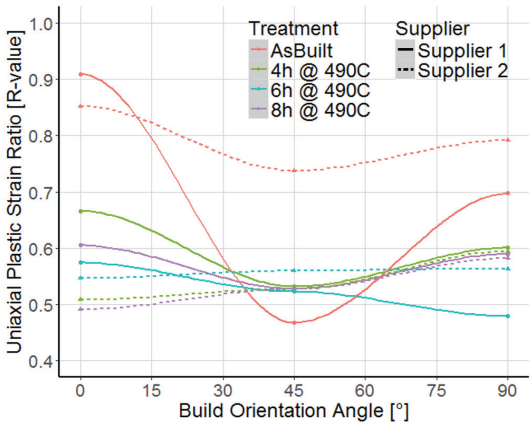

Figure 8: Plot of R-values versus build orientation angle, evaluated at 1.5% axial strain. The trend patterns for individual specimens are displayed using local polynomial regression fitting.

Further evaluation of plastic anisotropy has been performed via the DIC obtained R-value measurements, for which the obtained results are presented in Figure 8. The plot confirms (i) the existence of non-uniform transverse straining since $R_{isotropic} = 1$; and (ii) the variation of R-value between AM build orientation angles. Greater R-value variation is observed in Supplier 1 as-built and aged specimens (solid lines) which have been fabricated with the 67° laser-scan strategy. The harmonious and significantly flatter trends observed in Supplier 2 specimens (dashed lines) indicate a uniformity of plastic strain behaviour between build angles and suggests that a 90° scan strategy provides a more homogeneous microstructure. Regardless of the scan strategy, build orientation or heat treatment, all AM fabricated specimens displayed R-values < 1 signifying greater thinning in specimen's thickness direction whilst under tensile loading. This suggests the dominance of a systemic process anisotropy which cannot be abolished simply by aging the AM fabricated alloy. This inherent anisotropy stems from (i) the layer-wise deposition of powder; (ii) planar movement of the heat-source; and (iii) uni-axial movement of the build platform during fabrication. To abolish any fabrication manifested microstructural patterning it may therefore be necessary to perform a solubilization treatment step prior to aging. This re-crystallisation step has been shown to homogenise the AM MS300 microstructure by replacing laser scan tracks and melt-pool solidification pat-

terns with slender packets of parallel lath martensite through moderation of the alloy's solidification cooling rates [15, 2, 20, 38]. However, such circumstances incur additional processing cost, complexity, and time, which subtracts from the overall AM MS300 appeal.

3.4. Anisotropic yield function

Using the experimental data gathered from the tensile tests, it is possible to develop the parameters required to employ an anisotropic yield function. A widely used anisotropic yield function is Hill [42] with Hill's yield criterion equivalent stress given as,

$$\bar{\sigma} = \sqrt{F\left(\sigma_2 - \sigma_3\right)^2 + G\left(\sigma_3 - \sigma_1\right)^2 + H\left(\sigma_1 - \sigma_2\right)^2 + 2L\sigma_{23}^2 + 2M\sigma_{31}^2 + 2N\sigma_{12}^2} \tag{4}$$

where σ_{ij} is the stress component and F, G, H, L, M, and N are the Hill's coefficients. These coefficients can be calculated using tensile and shear yield stress in conjunction with a reference tensile and shear yield stress,

$$\begin{aligned} F &= \frac{\left(\sigma^0\right)^2}{2}\left[\frac{1}{\left(\sigma_2^y\right)^2} + \frac{1}{\left(\sigma_3^y\right)^2} - \frac{1}{\left(\sigma_1^y\right)^2}\right] \\ G &= \frac{\left(\sigma^0\right)^2}{2}\left[\frac{1}{\left(\sigma_3^y\right)^2} + \frac{1}{\left(\sigma_1^y\right)^2} - \frac{1}{\left(\sigma_2^y\right)^2}\right] \\ H &= \frac{\left(\sigma^0\right)^2}{2}\left[\frac{1}{\left(\sigma_1^y\right)^2} + \frac{1}{\left(\sigma_2^y\right)^2} - \frac{1}{\left(\sigma_3^y\right)^2}\right] \\ L &= \frac{3\left(\tau^0\right)^2}{2\left(\tau_{23}^y\right)^2} \\ M &= \frac{3\left(\tau^0\right)^2}{2\left(\tau_{31}^y\right)^2} \\ N &= \frac{3\left(\tau^0\right)^2}{2\left(\tau_{12}^y\right)^2} \end{aligned} \tag{5}$$

where σ_1^y, σ_2^y and σ_3^y are the tensile yield stresses, τ_{23}^y, τ_{31}^y and τ_{12}^y are the shear yield stresses, σ^0 and τ^0 are tensile and shear stresses respectively.

If the tensile reference yield stress is taken as the yield in the 0° orientation,

Eq. 5 can be rewritten as,

$$\begin{aligned} F &= \frac{1}{2}\left[\frac{1}{R_{22}^2}+\frac{1}{R_{33}^2}-\frac{1}{R_{11}^2}\right] \\ G &= \frac{1}{2}\left[\frac{1}{R_{33}^2}+\frac{1}{R_{11}^2}-\frac{1}{R_{22}^2}\right] \\ H &= \frac{1}{2}\left[\frac{1}{R_{11}^2}+\frac{1}{R_{22}^2}-\frac{1}{R_{33}^2}\right] \\ L &= \frac{3}{2R_{23}^2} \\ M &= \frac{3}{2R_{31}^2} \\ N &= \frac{3}{2R_{12}^2} \end{aligned} \tag{6}$$

where R_{ij} is the anisotropic yield stress ratio.

In addition to the yield stresses the Hill's coefficients can also be estimated using Lankford coefficients,

$$F = \frac{r_0}{r_{90}\left(r_0+r_1\right)};\quad G = \frac{1}{r_0+r_1};\quad N = \frac{\left(1+2r_{45}\right)\left(r_0+r_{45}\right)}{2r_{90}\left(1+r_0\right)} \tag{7}$$

Since the experimental data does not contain knowledge of the tensile yield strength in the x-direction nor shear stress, R_{11}, R_{23}, R_{31}, and R_{12} the relationships in Eq. 5 cannot be independently used, instead, using the relationships in Eq. 8 R_{11} and R_{23} can be estimated,

$$R_{11} = \sqrt{\frac{r_{90}\left(r_0+1\right)}{r_{90}\left(r_0+3\right)-\left(r_0+r_{90}\right)}}\quad R_{23} = \sqrt{\frac{3\left(r_0+1\right)r_{90}}{\left(2r_{45}+1\right)\left(r_0+r_{90}\right)}} \tag{8}$$

Using the approach taken by Bagherzadeh et al. [43], without further experimental understanding, it is reasonable to assume that the ratio of shear stresses τ_{31} and τ_{12} to the reference shear stress is 1, which results in $R_{12} = R_{31} = 1$. Applying this method to all gathered experimental data leads to the development of Table 4 which lists Hill's coefficients.

Table 4: Hill48 coefficients extracted from experimental data for both Supplier 1 and 2 for each corresponding heat treatment.

Data	**Heat-Treatment**	$\boldsymbol{F}$	$\boldsymbol{G}$	$\boldsymbol{H}$	$\boldsymbol{L}$	$\boldsymbol{M}$	$\boldsymbol{N}$
Supplier 1	As-Built	0.798	0.638	0.202	1.167	1.5	1.5
	4h @ $490°C$	0.58	0.514	0.42	1.306	1.5	1.5
	6h @ $490°C$	0.567	0.441	0.433	1.428	1.5	1.5
	8h @ $490°C$	0.539	0.522	0.461	1.398	1.5	1.5
Supplier 2	As-Built	0.747	0.705	0.253	1.387	1.5	1.5
	4h $490°C$	0.492	0.589	0.508	1.263	1.5	1.5
	6h $490°C$	0.502	0.522	0.498	1.35	1.5	1.5
	8h $490°C$	0.444	0.549	0.556	1.27	1.5	1.5

Using the Table 4 data, the following tensor representation can be constructed for each supplier and corresponding heat treatment which can be used in constitutive model development,

$$\bar{\sigma} = \sqrt{(\boldsymbol{P}\boldsymbol{\sigma}) \cdot \boldsymbol{\sigma}}; \quad \boldsymbol{P} = \begin{bmatrix} G+H & -H & -G & 0 & 0 & 0 \\ -H & F+H & -F & 0 & 0 & 0 \\ -G & -F & F+G & 0 & 0 & 0 \\ 0 & 0 & 0 & 2L & 0 & 0 \\ 0 & 0 & 0 & 0 & 2M & 0 \\ 0 & 0 & 0 & 0 & 0 & 2N \end{bmatrix} \tag{9}$$

3.5. Elasticity modulus

Values for Poisson ratio and elasticity modulus at 0° and 90° orientations were directly measured; these values for Poisson ratio were ν_{23} and ν_{32}, and values for elasticity modulus were E_2 and E_3. However, using information from the experimental data collected for the 45° orientation, the values of other Poisson ratios, elasticity modulus, and shear modulus can be estimated. The method of calculation of these values will be demonstrated based on the experimental values developed for Supplier 1/As-Built. To do this, firstly consider Hooke's law for an orthotropic material,

$$\begin{bmatrix} \varepsilon_1 \\ \varepsilon_2 \\ \varepsilon_3 \\ 2\varepsilon_4 \\ 2\varepsilon_5 \\ 2\varepsilon_6 \end{bmatrix} = \begin{bmatrix} \frac{1}{E_1} & -\frac{\nu_{21}}{E_2} & -\frac{\nu_{31}}{E_3} & 0 & 0 & 0 \\ -\frac{\nu_{12}}{E_1} & \frac{1}{E_2} & -\frac{\nu_{32}}{E_3} & 0 & 0 & 0 \\ -\frac{\nu_{13}}{E_1} & -\frac{\nu_{23}}{E_2} & \frac{1}{E_3} & 0 & 0 & 0 \\ 0 & 0 & 0 & \frac{1}{G_{23}} & 0 & 0 \\ 0 & 0 & 0 & 0 & \frac{1}{G_{13}} & 0 \\ 0 & 0 & 0 & 0 & 0 & \frac{1}{G_{12}} \end{bmatrix} \begin{bmatrix} \sigma_1 \\ \sigma_2 \\ \sigma_3 \\ \sigma_4 \\ \sigma_5 \\ \sigma_6 \end{bmatrix} \tag{10}$$

where ε_i are components of strain, σ_i are components of stress, E_i are the elasticity modulus in the direction of loading, ν_{ij} are the Poisson ratios calculated

based on extension in i and contraction in j, and G_{ij} are the shear modulus in direction j on the plane whose normal is in direction i.

Values of ϕ and θ can be used to define the orientation of a general plane as demonstrated by Figure 9 which gives the normal vector to the plane. This information can be used to generate strain tensors for the orientations of the material under investigation in this study, by rotating the plane to ensure the normal to the plane is in the direction of loading of interest.

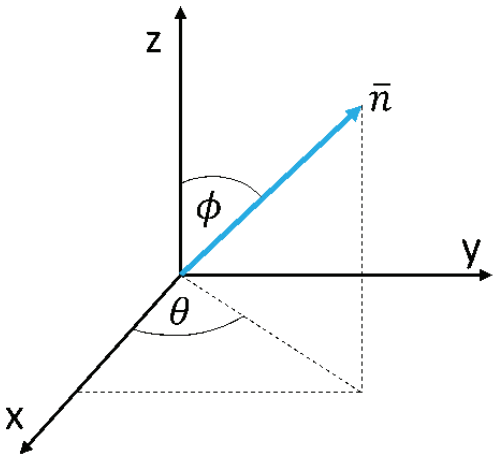

Figure 9: Normal vector to the plane under investigation.

The rotation matrix based on this relationship is provided in Eq. 11.

$$M = \begin{bmatrix} \cos\theta\sin\phi & \sin\theta\sin\phi & \cos\phi \\ -\sin\theta & \cos\theta & 0 \\ -\cos\theta\cos\phi & -\sin\theta\cos\phi & \sin\phi \end{bmatrix} \tag{11}$$

Using the rotation matrix given in Eq. 11, the rotated strain tensor can be calculated,

$$\varepsilon'_{ij} = M\varepsilon_{ij}M^T \tag{12}$$

where M^T is the transpose of the rotation matrix.

The strains which give a uni-axial loading condition in the rotated orientations can be calculated by first considering the uni-axial strain in the rotated state. Firstly, starting with the uni-axial strains in the x-direction,

$$\begin{aligned} \varepsilon'_1 &= \frac{\sigma_1}{E_1} \\ \varepsilon'_2 &= -\nu_{12}\varepsilon_1 \\ \varepsilon'_3 &= -\nu_{13}\varepsilon_1 \\ \varepsilon'_4,\ \varepsilon'_5,\ \varepsilon'_6 &= 0 \end{aligned} \tag{13}$$

Given a small amount of vertical strain (ε_3=0.005) the strains can be developed as,

$$\begin{aligned} \varepsilon_1' &= 0.005 \\ \varepsilon_2' &= -0.005\nu_{12} \\ \varepsilon_3' &= -0.005\nu_{13} \\ \varepsilon_4',\ \varepsilon_5',\ \varepsilon_6' &= 0 \end{aligned} \tag{14}$$

Using components of the rotated strain tensor, ε_{ij}' in Eq. 14 and equating that with the relationship developed for the un-rotated strains gives,

$$\begin{aligned} 0.005 = \varepsilon_1 \cos^2\theta \sin^2\phi + \varepsilon_2 \sin^2\phi \sin^2\theta + \varepsilon_3 \cos^2\phi + 2\varepsilon_4 \sin^2\phi \sin\theta\cos\theta \\ +2\varepsilon_6 \sin\theta \sin\phi\cos\phi + 2\varepsilon_5 \cos\theta\cos\phi\sin\phi \end{aligned}$$

$$-0.005\nu_{12} = \varepsilon_1 \sin^2\theta + \varepsilon_2 \cos^2\theta - 2\varepsilon_4 \sin\theta\cos\theta$$

$$\begin{aligned} -0.005\nu_{13} = \varepsilon_1 \cos^2\phi\cos^2\theta + \varepsilon_2 \cos^2\phi \sin^2\theta + \varepsilon_3 \sin^2\phi + 2\varepsilon_4 \cos^2\phi \sin\theta\cos\theta \\ -2\varepsilon_3 \sin\phi\cos\phi\cos\theta - 2\varepsilon_6 \sin\phi\cos\phi\sin\theta \end{aligned}$$

$$\begin{aligned} 0 = -2\varepsilon_1 \cos\theta\sin\phi\sin\theta + 2\varepsilon_2 \sin\phi\sin\theta\cos\theta + 2\varepsilon_4 \left(\cos^2\theta\sin\phi - \sin\theta\sin^2\theta\right) \\ -2\varepsilon_5 \sin\theta\cos\phi - 2\varepsilon_6 \cos\theta\cos\phi \end{aligned}$$

$$\begin{aligned} 0 = -2\varepsilon_1 \cos^2\theta\sin\phi\cos\phi - 2\varepsilon_2 \sin^2\theta\cos\phi\sin\phi + 2\varepsilon \sin\phi\cos\phi \\ -4\varepsilon_4 \sin\theta\sin\phi\cos\phi\cos\theta - 2\varepsilon_5 \left(\cos^2\phi\cos\theta + \cos\theta\sin^2\phi\right) \\ +2\epsilon_6 \left(-\cos^2\phi\sin\theta + \sin^2\phi\sin\theta\right) \end{aligned}$$

$$\begin{aligned} 0 = 2\varepsilon_1 \sin\theta\cos\phi\cos\theta - 2\varepsilon_2 \cos\phi\sin\theta\cos\theta + 1\varepsilon_4 \left(\sin^2\theta\cos\phi - \cos^2\theta\cos\phi\right) \\ -2\varepsilon_5 \sin\theta\sin\phi + 2\varepsilon_6 \sin\phi\cos\theta \end{aligned} \tag{15}$$

The angles of ϕ and θ for the orientations of the samples under investigation are listed in Table 5.

Table 5: Values for angles to define the orientation of the plane under investigation.

Specimen Orientation	$\boldsymbol{\phi}$	$\boldsymbol{\theta}$
Horizontal (0°)	90°	90°
Inclined (45°)	0°	90°
Vertical (90°)	45°	90°

Using these orientations, the components of un-rotated strain which give uni-axial loading at the directions of interest can be solved using Eq. 15, which

are given in Eq. 16.

$$
\begin{aligned}
&\text{Horizontal } (0^\circ)\\
&\qquad \varepsilon_1 = -0.005\nu_{12}\\
&\qquad \varepsilon_2 = 0.005\\
&\qquad \varepsilon_3 = -0.005\nu_{13}\\
&\qquad \varepsilon_4\ \varepsilon_5,\ \varepsilon_6 = 0\\
&\text{Inclined } (45^\circ)\\
&\qquad \varepsilon_1 = -0.005\nu_{12}\\
&\qquad \varepsilon_2 = 0.0025\,(1-\nu_{13})\\
&\qquad \varepsilon_3 = 0.0025\,(1-\nu_{13})\\
&\qquad \varepsilon_4 = 0\\
&\qquad \varepsilon_5 = 0\\
&\qquad \varepsilon_6 = 0.0025\,(\nu_{13}+1)\\
&\text{Vertical } (0^\circ)\\
&\qquad \varepsilon_1 = -0.005\nu_{12}\\
&\qquad \varepsilon_2 = -0.005\nu_{13}\\
&\qquad \varepsilon_3 = 0.005\\
&\qquad \varepsilon_4.\ \varepsilon_5,\ \varepsilon_6 = 0
\end{aligned}
\tag{16}
$$

Using the orthotropic equation for Hooke's law in Eq. 10 and the strains in Eq. 16, the corresponding un-rotated stresses can be obtained for each orientation using the experimental knowledge that $E_2 = 161$GPa and $E_3 = 122$GPa, and $\nu_2 3 = 0.24$ and $\nu_3 2 = 0.35$. The stresses can then be rotated to achieve uni-axial loading in the orientation under investigation using Eq. 17.

$$\sigma'_{ij} = M_{ij}\sigma_{ij}M^T_{ij} \tag{17}$$

Using the rotated stresses and the equivalent stress equations, the uni-axial

loading can obtained for each orientation,

Horizontal (0°)

$$\bar{\sigma} = \sqrt{F\left(\sigma_2' - \sigma_3'\right)^2 + G\left(\sigma_3' - \sigma_1'\right)^2 + H\left(\sigma_1' - \sigma_2'\right)^2 + 2L{\sigma_{23}'}^2 + 2M{\sigma_{31}'}^2 + 2N{\sigma_{12}'}^2} = 0.005E_2$$

Inclined (45°)

$$\bar{\sigma} = \sqrt{F\left(\sigma_2' - \sigma_3'\right)^2 + G\left(\sigma_3' - \sigma_1'\right)^2 + H\left(\sigma_1' - \sigma_2'\right)^2 + 2L{\sigma_{23}'}^2 + 2M{\sigma_{31}'}^2 + 2N{\sigma_{12}'}^2} = 0.005E_{45}$$

Vertical (90°)

$$\bar{\sigma} = \sqrt{F\left(\sigma_2' - \sigma_3'\right)^2 + G\left(\sigma_3' - \sigma_1'\right)^2 + H\left(\sigma_1' - \sigma_2'\right)^2 + 2L{\sigma_{23}'}^2 + 2M{\sigma_{31}'}^2 + 2N{\sigma_{12}'}^2} = 0.005E_3$$

Horizontal(0°) (x-direction)

$$\bar{\sigma} = \sqrt{F\left(\sigma_2' - \sigma_3'\right)^2 + G\left(\sigma_3' - \sigma_1'\right)^2 + H\left(\sigma_1' - \sigma_2'\right)^2 + 2L{\sigma_{23}'}^2 + 2M{\sigma_{31}'}^2 + 2N{\sigma_{12}'}^2} = 0.005E_1 \quad (18)$$

This provides four equations in terms of the unknowns, ν_{12}, ν_{21}, ν_{13}, ν_{31}, G_{23}, E_1. The method applied to solve these equations for the unknowns was using an optimisation strategy. In this work a genetic algorithm was employed to trial values of the unknowns to reach minimum of the fitness function which contained the equations in Eq 18. The solution arrived at for these parameters is given in Table 6.

Table 6: Possible solution to the unknowns estimated using a genetic algorithm optimisation.

$\boldsymbol{\nu_{12}}$	$\boldsymbol{\nu_{21}}$	$\boldsymbol{\nu_{13}}$	$\boldsymbol{\nu_{31}}$	$\boldsymbol{G_{23}}$ **(GPa)**	$\boldsymbol{E_1}$ **(GPa)**
0.43	0.93	0.26	0.01	123	137

What needs to be appreciated by this approach is there are a range of values these unknowns can take; therefore, the values determined are the best combination of the parameters and not necessary the exact values. Consequently, using the experimental knowledge gained in this work, the orthotropic elasticity modulus of the best combination of parameters can be given. This is only an approximation but does allow the opportunity to successfully apply an elasticity modulus when using this material in computational analyses. Therefore, the

total elasticity modulus is given as,

$$E_{ij} = \begin{bmatrix} \frac{1}{137} & \frac{-93}{16100} & \frac{-1}{12200} & 0 & 0 & 0 \\ \frac{-43}{13700} & \frac{1}{161} & \frac{-7}{24400} & 0 & 0 & 0 \\ \frac{-13}{6850} & \frac{-6}{4025} & \frac{1}{122} & 0 & 0 & 0 \\ 0 & 0 & 0 & \frac{1}{123} & 0 & 0 \\ 0 & 0 & 0 & 0 & \frac{1}{G_{13}} & 0 \\ 0 & 0 & 0 & 0 & 0 & \frac{1}{G_{12}} \end{bmatrix} \tag{19}$$

Applying this method across all gathered experimental data gives Table 7.

Table 7: Components of the orthotropic Hooke's law tensor for the two suppliers at different heat treatments. The missing experimental data used to develop this table was arrived at using the theoretical understanding outlined and an optimisation strategy.

Heat-Treatment	E_1 (GPa)	E_2 (GPa)	E_3 (GPa)	G_{23} (GPa)	ν_{12}	ν_{21}	ν_{13}	ν_{31}	ν_{23}	ν_{32}
				Supplier 1						
As-Built	137	161	122	122	0.43	0.93	0.26	0.01	0.24	0.35
4h @ $490^\circ C$	183	182	180	132	0.34	0.24	0.49	0.01	0.33	0.32
6h @ $490^\circ C$	174	178	178	142	0.32	0.11	0.22	0.18	0.4	0.28
8h @ $490^\circ C$	172	183	180	159	0.3	0.45	0.32	0.81	0.34	0.32
				Supplier 2						
As-Built	117	150	120	104	0.5	0.29	0.19	0.36	0.34	0.38
4h @ $490^\circ C$	173	170	171	143	0.41	0.56	0.19	0.38	0.29	0.31
6h @ $490^\circ C$	145	174	172	118	0.15	0.35	0.69	0.27	0.3	0.34
8h @ $490^\circ C$	150	179	170	148	0.06	0.07	0.28	0.72	0.38	0.34

4. Conclusions

The deficit of process knowledge concerning the factors which influence the mechanical performance of AM metals is forestalling the technology's widespread advancement into the engineering arena, since components destined for use in demanding engineering applications have rigid requirements and specifications, and a strict precision is necessary for their manufacture. Accordingly, this research article investigates inconsistencies in the mechanical characteristics and plastic anisotropy levels in identical EOSINT M280 fabricated MS300 test-coupons that have been supplied by two AM facilities. Three build orientations (0°,45°, and 90°) are investigated, and the alloy's performance has been monitored in the as-built and aged conditions (4h, 6h and 8h at $490^\circ C$). The important conclusions are summarized as follows:

1. Considerable microstructural dissimilarities affecting mechanical performance and anisotropy have been observed in as-built MS300 samples obtained from alternative suppliers;
2. The AM laser scan strategy, and in particular the scan rotation angle between AM build layers, had a profound effect on the strength, ductility and anisotropy (transverse strain behaviour) developed in the as-built alloy;
3. Microstructural porosities and un-fused powder particles observed in one group of samples led to reduced plasticity and erratic fracture behaviours in aged MS300 samples;

4. The AM component's relative density is affected by unfavourable powder feedstock characteristics (size and morphology), and the part's cross-sectional projection onto the build-platform;
5. Plastic anisotropy can be reduced significantly through application of a dislocation hindering precipitation heat-treatment, however, a degree of transverse strain anisotropy is likely to remain due to the AM material's fabrication history.

Acknowledgement

This research project has been jointly funded by the Irish Research Council (IRC), through the Government of Ireland Postgraduate Research Programme, and the Faculty of Science and Engineering of the University of Limerick. The authors are grateful to the staff of Thermo Fisher Scientific for their support with data analysis.

Data availability

The raw/processed data required to reproduce these findings cannot be shared at this time as the data also forms part of an ongoing study.

References

[1] E. A. Jägle, Z. Sheng, L. Wu, L. Lu, J. Risse, A. Weisheit, D. Raabe, Precipitation reactions in age-hardenable alloys during laser additive manufacturing, JOM 68 (2016) 943–949.

[2] R. Casati, J. Lemke, A. Tuissi, M. Vedani, Aging behaviour and mechanical performance of 18-ni 300 steel processed by selective laser melting, Metals 6 (2016).

[3] D. Croccolo, M. De Agostinis, S. Fini, G. Olmi, F. Robusto, K. Ciric, A. Vranic, N. Bogojevic, Fatigue response of as-built dmls maraging steel and effects of aging, machining, and peening treatments, Metals 8 (2018).

[4] D. Herzog, V. Seyda, E. Wycisk, C. Emmelmann, Additive manufacturing of metals, Acta Materialia 117 (2016) 371 – 392.

[5] B. Klahn, C.and Leutenecker, M. Meboldt, Design strategies for the process of additive manufacturing, Procedia CIRP 36 (2015) 230 – 235. CIRP 25th Design Conference Innovative Product Creation.

[6] S. Moylan, J. Slotwinski, Assessment of guidelines for conducting round robin studies in additive manufacturing, in: 2014 ASPE Spring Topical Meeting–Dimensional Accuracy and Surface Finish in Additive Manufacturing, volume 57, NIST, Berkelye, CA, 2014, pp. 1–4.

[7] S. Moylan, J. Land, A. Possolo, Additive manufacturing round robin protocols: A pilot study, in: Proceedings of the Solid Freeform Fabrication Symposium, Solid Freeform Fabrication Symposium, NIST, Austin, TX, 2015, pp. 1–9. URL: https://www.nist.gov/publications/additive-manufacturing-round-robin-protocols-pilot-study.

[8] B. Ahuja, A. Schaub, D. Junker, M. Karg, F. Tenner, R. Plettke, M. Merklein, M. Schmidt, A round robin study for leaser beam melting in a metal powder bed, South African Journal of Industrial Engineering 27 (2016) 30–42.

[9] D. Koutney, L. Panteljev, J. Tomes, D. Palousek, Comparison of selective laser melting of 18ni maraging steel by pxl and m2 cusing, MM (Modern Machinery) Science Journal (2016) 1590–1596.

[10] M. Frey, M. Shellabear, L. Thersson, Mechanical Testing of DMLS Parts, White Paper, Electro Optical Systems (EOS), 2015. URL: http://www.fabricadeprototipos.com/links/DMLS/link2_ensaiosmecanicos.pdf.

[11] EOS, EOS MaragingSteel MS1, Material data sheet EOSINT M280 EOSINT M270, Electro Optical Systems (EOS), 2011. URL: http://ip-saas-eos-cms.s3.amazonaws.com/public/1af123af9a636e61/042696652ecc69142c8518dc772dc113/EOS_MaragingSteel_MS1_en.pdf.

[12] K. Monkova, I. Zetkova, L. Kučerová, M. Zetek, P. Monka, M. Daňa, Study of 3d printing direction and effects of heat treatment on mechanical properties of ms1 maraging steel, Archive of Applied Mechanics (2018) 1–14.

[13] J. Sedlak, D. Rican, M. Piska, L. Rozkosny, Study of materials produced by powder metallurgy using classical and modern additive laser technology, Procedia Engineering 100 (2015) 1232–1241. Part of Special issue 25th DAAAM International Symposium on Intelligent Manufacturing and Automation, 2014.

[14] M. Stanford, K. Kibble, M. Lindop, D. Mynors, C. Durnall, An investigation into fully melting a maraging steel using direct metal laser sintering (dmls), in: Special Edition Metal Forming Conference 2008, 79, 2008, pp. 847–852.

[15] T. Becker, D. Dimitrov, The achievable mechanical properties of slm produced maraging steel 300 components, Rapid Prototyping Journal 22 (2016) 487–494.

[16] K. Kempen, E. Yasa, L. Thijs, J.-P. Kruth, J. Van Humbeeck, Microstructure and mechanical properties of selective laser melted 18ni-300 steel, Physics Procedia 12 (2011) 255 – 263. Lasers in Manufacturing 2011 - Proceedings of the Sixth International WLT Conference on Lasers in Manufacturing.

[17] T. Burkert, A. Fischer, The effects of heat balance on the void formation within marage 300 processed by selective laser melting, in: • (Ed.), International Solid Freeform Fabrication Symposium, University of Texas, 2015, pp. 745–757. URL: http://sffsymposium.engr.utexas.edu/sites/default/files/2015/2015-61-Burkert.pdf.

[18] J. Suryawanshi, K. Prashanth, U. Ramamurty, Tensile, fracture, and fatigue crack growth properties of a 3d printed maraging steel through selective laser melting, Journal of Alloys and Compounds 725 (2017) 355 – 364.

[19] C. Tan, K. Zhou, W. Ma, P. Zhang, M. Liu, T. Kuang, Microstructural evolution, nanoprecipitation behavior and mechanical properties of selective laser melted high-performance grade 300 maraging steel, Materials and Design 134 (2017) 23 – 34.

[20] J. Mutua, S. Nakata, T. Onda, Z. Chen, Optimization of selective laser melting parameters and influence of post heat treatment on microstructure and mechanical properties of maraging steel, Materials and Design 139 (2018) 486 – 497.

[21] ASTM, ASTME8/E8M-16a: Standard Test Methods for Tension Testing of Metallic Materials, Test Standard, ASTM, 2016. URL: http://www.astm.org/cgi-bin/resolver.cgi?E8E8M-16a. doi:10.1520/E0008_E0008M-16A.

[22] W. Sha, Z. Guo, Maraging Steels, Modelling of Microstructure, Properties and Applications, Woodhead Publishing, Cambridge UK, 2009. ISBN: 978-1-84569-686-3.

[23] R. Casati, J. Lemke, M. Vedani, Microstructural and mechanical properties of as built, solution treated and aged 18 ni (300 grade) maraging steel produced by selective laser melting, La Metallurgia Italiana (2017) 11–20.

[24] E. Jägle, P. Choi, J. Van Humbeeck, D. Raabe, Precipitation and austenite reversion behavior of a maraging steel produced by selective laser melting, Journal of Materials Research 29 (2014) 2072–2079.

[25] ASTM, ASTMB962-17: Standard Test Methods for Density of Compacted or Sintered Powder Metallurgy (PM) Products Using Archimedes' Principle, Test Standard, ASTM, 2017.

[26] ThermoScientific, Thermo Scientific Avizo Software 9, User's Guide 9, ThermoScientific, Berlin, DE, 2018. Https://www.fei.com/WorkArea/DownloadAsset.aspx?id=34359741225.

[27] ASTM, ASTME92-17: Standard Test Methods for Vickers Hardness and Knoop Hardness of Metallic Materials, Test Standard, ASTM, 2017. URL: https://www.astm.org/Standards/E92.htm.

[28] R Core Team, R: A Language and Environment for Statistical Computing, Software Application, R Foundation for Statistical Computing, Vienna, Austria, 2014. URL: http://www.R-project.org/.

[29] LaVision, Full Field Strain Measurement, Subject Guide, La Vision GmbH, 2014. URL: http://www.lavision.de/en/applications/materials-testing/stereo-dic/index.php.

[30] ASTM, ASTME132-04: Standard Test Method for Poisson's Ratio at Room Temperature, Test Standard, ASTM, 2004. URL: http://www.astm.org/cgi-bin/resolver.cgi?E132-04. doi:10.1520/E0132-04.

[31] ASTM, ASTME517-18: Standard Test Method for Plastic Strain Ratio r for Sheet Metal, Test Standard, ASTM, 2018. URL: https://www.astm.org/Standards/E517.htm. doi:10.1520/E0517-18.

[32] S. Yin, C. Chen, X. Yan, X. Feng, R. Jenkins, P. O'Reilly, M. Liu, H. Li, R. Lupoi, The influence of aging temperature and aging time on the mechanical and tribological properties of selective laser melted maraging 18ni-300 steel, Additive Manufacturing 22 (2018) 592 – 600.

[33] P. Quinn, S. O'Halloran, J. Lawlor, R. Raghavendra, Characterization of recycled powders and resulting properties derived from additive manufacturing, in: Preliminary Proceedings: 35th International Manufacturing Conference (IMC35), 35, Dublin Institute of Technology, 2018, pp. 8–11.

[34] A. Sutton, C. Kriewall, M. Leu, J. Newkirk, Powders for additive manufacturing processes: Characherization techniques and effects on part properties, in: Proceedings of the 26th Annual International Solid Freeform Fabrication Symposium, Solid Freeform Fabrication 2016, 2016, pp. 3–29.

[35] F. Lang, N. Kenyon, WRC Bulletin: Welding of Maraging Steels, Technical Report 159, Welding Research Council, USA, 1971.

[36] ASTM, ASTME140-07: Standard Hardness Conversion Tables for Metals Relationship Among Brinell Hardness, Vickers Hardness, Rockwell Hardness, Superficial Hardness, Knoop Hardness, and Scleroscope Hardness, Test Standard, ASTM, 2007. URL: http://www.astm.org/cgi-bin/resolver.cgi?E140-07. doi:10.1520/E0140-07.

[37] U. Viswanathan, G. Dey, V. Sethumadhavan, Effects of austenite reversion during overageing on the mechanical properties of 18 ni (350) maraging steel, Materials Science and Engineering: A 398 (2005) 367 – 372.

[38] Y. Bai, Y. Yang, D. Wang, M. Zhang, Influence mechanism of parameters process and mechanical properties evolution mechanism of maraging steel 300 by selective laser melting, Materials Science and Engineering: A 703 (2017) 116 – 123.

[39] R. Branco, J. Costa, F. Berto, S. M. J. Razavi, J. A. M. Ferreira, C. Capela, L. Santos, F. Antunes, Low-cycle fatigue behaviour of aisi 18ni300 maraging steel produced by selective laser melting, Metals 8 (2018).

[40] M. Ashby, D. Jones, Engineering Materials 2: An Introduction to Microstructures, Processing and Design, Butterworth-Heinemann, New York USA, 2005. ISBN: 9780080468631.

[41] B. Hutchinson, Critical assessment 16: Anisotropy in metals, Materials Science and Technology 31 (2015) 1393–1401.

[42] R. Hill, A theory of the yielding and plastic flow of anisotropic metals, Proceedings of the Royal Society of London. Series A, Mathematical and Physical Sciences 193 (1948) 281–297.

[43] S. Bagherzadeh, M. Mirnia, B. Mollaei Dariani, Numerical and experimental investigations of hydro-mechanical deep drawing process of laminated aluminum/steel sheets, Journal of Manufacturing Processes 18 (2015) 131 – 140.